Retrieval of Aerosol Combined with Assimilated Forecast

Mayumi Yoshida[1], Keiya Yumimoto[2], Takashi M. Nagao[3], Taichu Tanaka[4], Maki Kikuchi[5], Hiroshi Murakami[5]

[1]Remote Sensing Technology Center of Japan, Tsukuba, 305-8505, Japan
5 [2]Research Institute for Applied Mechanics, Kyushu University, Fukuoka, 816-8580, Japan
[3]Atmosphere and Ocean Research Institute, University of Tokyo, Kashiwa, 277-8568, Japan
[4]Meteorological Research Institute, Tsukuba, 305-0052, Japan
[5]Japan Aerospace Exploration Agency, Tsukuba, 305-8505, Japan

10 *Correspondence to*: Mayumi Yoshida (mayum@restec.or.jp)

Abstract. We developed a new aerosol retrieval algorithm combining a numerical aerosol forecast. In the retrieval algorithm, the short-term forecast from an aerosol data assimilation system was used for a priori estimate instead of spatially and temporally constant values. This method was demonstrated using the Advanced Himawari Imager onboard the Japan Meteorological Agency's geostationary satellite Himawari-8, and the results showed spatially finer distributions than the
15 model forecast and less noisy distributions than the original algorithm. We validated the new algorithm using ground observation data and found that the aerosol parameters detectable by satellite sensors were retrieved more accurately than a priori model forecast by adding satellite information. Moreover, the retrieval accuracy was improved by using the model forecast as compared with using constant a priori estimates. By using the assimilated forecast for a priori estimate, information from previous observations can be propagated to future retrievals, thereby leading to better retrieval accuracy.
20 Observational information from the satellite and aerosol transport by the model is incorporated cyclically to effectively estimate the optimum field of aerosol.

1 Introduction

Airborne aerosols have impacts on air quality and human health. Aerosols also influence the energy budget of the earth's climate system through the scattering and absorption of solar radiation. The fifth assessment report of the Intergovernmental
25 Panel on Climate Change (IPCC 2014) stated that radiative forcing of the total aerosol effect in the atmosphere, including cloud adjustments due to aerosols, is –0.9 W m^{-2}. The report also showed, however, that the range of uncertainties in radiative forcing remains large (-1.9 W m^{-2} to -0.1 W m^{-2}). In order to estimate the impact of aerosols on climate systems, it is important to investigate the global distribution of aerosols using satellite observations, by taking advantage of the ability to observe the globe continuously, in addition to aerosol ground observation.

30

Various aerosol retrieval algorithms from satellite observations have been developed. However, not all aerosol properties can be accurately detected by satellite sensors, as there are more unknown aerosol parameters (e.g., particle size distributions, vertical density distribution, shape, refractive index) than the actual information obtained by satellite sensors. General studies use some assumptions or information about aerosol parameters, and limit the retrieval aerosol parameters. For example,

35 Higurashi and Nakajima (1999), and Fukuda et al. (2013) assumed fixed complex refractive indices (1.5 - 0.005i in Higurashi and Nakjima (1999), and $1.503 – 7.16 \times 10^{-8}i$ for small mode particles and $1.445 – 1.00 \times 10^{-8}i$ for coarse mode particles based on sulfate and sea spray models, respectively, in Fukuda et al. (2013)), and retrieved the aerosol optical thickness and Ångström exponent. Some studies assumed aerosol particle models according to the location and season. For example, Kaufman et al. (1997), Remer et al. (2005), and Levy et al. (2007) estimated the aerosol optical thickness and fine

40 mode fraction over a dark target using the Moderate Resolution Imaging Spectroradiometer (MODIS), by selecting the fine-dominate particle models as a function of geography and season. Hsu et al. (2004) retrieved the optical thickness and type of aerosols over desert regions using blue channels (< 500 nm), where the surface reflectance was relatively low, assuming dust or a mixture of dust and smoke depending on the region and season. Jeong et al. (2016) used a priori information according to the location and season. However, these studies did not take temporal changes into account. Because it is impossible to

45 completely fix aerosol type as a function of geography and season, unrealistic assumptions lead to one of the major causes of retrieval error.

Aerosol data assimilation studies using satellite data have also been developed to obtain better initial conditions for the aerosol transport model. The aerosol data assimilation study was first developed with low Earth orbit (LEO) satellites

50 (Benedetti et al., 2009; Saide et al., 2013; Dai et al., 2014; Rubin et al., 2015; Yumimoto et al., 2015). In recent years, assimilation studies have been conducted using geostationary satellites with large spatial coverage and fine observation frequencies (Saide et al., 2014; Lee et al., 2016; Yumimoto et al., 2016; Yumimoto et al., 2018; Die et al., 2019; Jin et al., 2019).

55 Due to the development of such assimilation studies, the satellite data have contributed to more accurate aerosol forecasts. However, no such study utilizes the assimilated model forecast of aerosol for a priori estimate of the retrieval. Since not all parameters can be accurately detected by satellite sensors, and unrealistic assumptions of aerosol parameters are a major cause of retrieval errors as mentioned above, adding the model information is expected to improve the retrieval accuracy. Therefore, in this study, we utilize the forecast of an aerosol transport model for a priori estimates of the retrieval. This

60 allows the aerosol information in the aerosol transport model to be used for retrieval. And by using the assimilated forecast, information from previous satellite observations can be propagated to future retrievals through the aerosol transport model.

Section 2 explains the retrieval methodology in detail. Section 3.1 presents the results of application to the Advanced Himawari Imager (AHI) onboard Himawari-8. Section 3.2 describes the validation of the products using ground observations, and Section 3.3 tests the worst-case scenario. And finally, Section 4 summarizes our findings.

2 Methodology

The aerosol retrieval algorithm applied in this study is based on Yoshida et al. (2018). Further, we use an aerosol forecast from the transport model that has been assimilated with previous satellite observations for a priori estimates of the retrieval. As the retrieval algorithm of Yoshida et al. (2018) can be applied to various imaging satellite sensors, the methodology explained in this section can also be applied to various sensors. However, this study first targets the Himawari-8/AHI with its assimilation system in place. The Himawari-8/AHI has six bands from the visible to near-infrared wavelength ranges, and observes the top of atmosphere radiance at a resolution of 0.5-2.0 km over Asia and Oceania at 10-min. intervals (Bessho et al., 2016).

Figure 1 depicts the process of using forecast data for a priori estimates of the retrieval. In the original retrieval process, the Level-2 (L2) aerosol optical thickness at 500 nm (τ), Ångström exponent between 400 and 600 nm (α), and single-scattering albedo at 500 nm (ω) are retrieved using Level-1 (L1) AHI-observed radiance every 10 minutes around time T0 as per Yoshida et al. (2018). The Level-3 (L3) τ and α at T0 are then estimated using L2 products in one hour by an hourly-combined algorithm (Kikuchi et al., 2018). The hourly-combined algorithm is a method that (1) minimizes cloud contamination using the difference between aerosol and cloud spatiotemporal variability characteristics, and (2) interpolates the aerosol retrievals using 1 h of data and the movement of clouds within the hour.

The L3 τ at T0 is then assimilated into a global aerosol transport model by the 2D-Var assimilation system (Yumimoto et al., 2018). For the aerosol transport model, we use MASINGAR (Model of Aerosol Species IN the Global AtmospheRe; Tanaka et al., 2003; Tanaka and Chiba, 2005) developed at the Meteorological Research Institute (MRI) of the Japan Meteorological Agency (JMA). MASINGAR covers the major tropospheric aerosol components (i.e., black and organic carbon, mineral dust (10-size bins), sea salt (10-size bins), sulfate aerosols)) and their precursors (e.g., sulfur dioxide (SO_2), dimethyl sulfide, terpenes)), and is coupled online with an atmospheric general circulation model (MRI-AGCM3; Yukimoto et al., 2012). The model's grid resolution is set to horizontal Gaussian TL479 (960 x 480 grids, about 0.375 degree) and 40 vertical layers in hybrid sigma-pressure coordinates from the ground to 0.4 hPa. The integration time step is set to 600 seconds. Anthropogenic emissions of SO_2, black and organic carbon are taken from the MACCity emission inventory (Granier et al., 2011). Daily biomass burning emission flux is taken from the Global Fire Assimilation System (GFAS, Kaiser et al., 2012) version 1.2 provided by the European Centre of Medium Range Forecast (ECMWF). The horizontal wind components and sea surface temperature are nudged toward the global analyses and forecasts of JMA (GANAL). The forecast from the

95 assimilation system serves as the operational sand and dust forecasting by JMA, the aerosol property model product in the JAXA Himawari Monitor (https://www.eorc.jaxa.jp/ptree/index.html), and a member of the ICAP multi-model ensemble (MME) (Xian et al., 2019). The volume concentration (then τ) of each aerosol component at the next time (T1) is then forecasted using the assimilated aerosol transport model.

100 In the new retrieval process, we retrieved the L2 aerosol properties (τ, α, and ω) from AHI-observed radiance at T1 using these L4 forecasts for a priori estimates of the retrieval. In this way, the information from previous observations at T0 is used for the next aerosol retrievals at T1 through the aerosol transport model. Figure 6 compares the improved retrieval results with the original retrieval results at T1.

105 The methodology for using the forecast as a priori estimates of the retrieval is detailed as follows: In the retrieval process, the final retrieval parameters (τ, α, and ω) are calculated from the set of aerosol parameters (τ, external mixing ratio of dry volume concentration for fine particles η_f, and imaginary part of refractive index for fine mode m_i) defined by Yoshida et al. (2018). We retrieve the aerosol parameters (τ, η_f, and m_i) using an optimal estimation method (Rodgers 2000). The state vector of a set of aerosol parameters $\boldsymbol{x} = \{\tau, \eta_f, m_i\}$ is derived by minimizing object function J (Eq. (1)). It uses the

110 measurement vector of a gas-corrected observed reflectance set $\boldsymbol{R} = \{\rho_i^{obs\prime}, = 1, ..., N\}$ and simulated TOA reflectance $\boldsymbol{F(x)} = \{\rho_i^{sim}, i = 1, ..., N\}$, where N is the channel number.

$$J = [\boldsymbol{R} - \boldsymbol{F(x)}]^T \boldsymbol{S_e}^{-1} [\boldsymbol{R} - \boldsymbol{F(x)}] + [\boldsymbol{x} - \boldsymbol{x_a}]^T \boldsymbol{S_a}^{-1} [\boldsymbol{x} - \boldsymbol{x_a}] \qquad (1)$$

where $\boldsymbol{x_a} = \left\{\tau_a, \eta_{f_a}, m_{i_a}\right\}$ is the vector of a prior estimate of $\boldsymbol{x}$, and $\boldsymbol{S_e}$ and $\boldsymbol{S_a}$ are the covariance matrices of $\boldsymbol{R}$ and $\boldsymbol{x_a}$, respectively. The calculations of $\boldsymbol{R}, \boldsymbol{F(x)}$, and $\boldsymbol{S_e}$ are the same as those of Yoshida et al. (2018), but we apply canonical

115 correlation analysis to find the optimal coordinate system, and converted $\boldsymbol{R}, \boldsymbol{F(x)}$, and $\boldsymbol{S_e}$ to the coordinate system whose dimension is reduced to the number of retrieved parameters (three). In the original retrieval process, we used spatially and temporally constant values of $\boldsymbol{x_a}$, and $\boldsymbol{S_a}$ that are derived from climate analysis, and assumed that the non-diagonal component of covariance matrices was set to 0 (Yoshida et al., 2018).

120 To introduce more realistic a prior estimate and covariances into the retrieval process, we employ the forecast from the aerosol assimilation system instead of the constants. The model forecast includes the total aerosol optical thickness at 500 nm and 870 nm, and the absorption aerosol optical thickness at 500 nm derived from the modeled volume concentration and extinction cross section of each aerosol component (Yumimoto et al., 2017). We assign a priori estimate $\boldsymbol{x_a}$ as follows: The model's total aerosol optical thickness at 500 nm is used for τ_a. η_{f_a} is derived from the ratio of total aerosol optical thickness between 500 nm and 870 nm. As the selection of m_{i_a}, we use the model's ω as calculated from the total and absorption

125 aerosol optical thickness at 500 nm.

The assimilation system uses an ensemble method to calculate the background error covariance matrix (Yumimoto et al., 2018). In the method, the ensemble was collected from forecast values within ±2 hours of the targeted hour of the five

130   previous forecasts (Fig. 2). We employ this method to define $\boldsymbol{S_a}$. The model ensemble enables $\boldsymbol{S_a}$ to include the non-diagonal component and express the error of aerosol transport. However, $\boldsymbol{S_a}$ from model ensemble may become too small when the model does not predict the aerosol event itself. For that reason, in order to estimate total $\boldsymbol{S_a}$, we add a model absolute error ($\boldsymbol{S_a^A}$) to the error estimated from the ensemble ($\boldsymbol{S_a^E}$) as follows:

$$\boldsymbol{S_a} = \boldsymbol{S_a^E} + \boldsymbol{S_a^A} = \begin{bmatrix} \sigma_{\tau_a}{}^2 & \sigma_{\tau_a \eta_{f_a}} & \sigma_{\tau_a m_{i_a}} \\ \sigma_{\tau_a \eta_{f_a}} & \sigma_{\eta_{f_a}}{}^2 & \sigma_{\eta_{f_a} \sigma_{m_{i_a}}} \\ \sigma_{\tau_a m_{i_a}} & \sigma_{\eta_{f_a} \sigma_{m_{i_a}}} & \sigma_{m_{i_a}}{}^2 \end{bmatrix},$$ (2)

135   $\sigma_{\tau_a} = \sigma_{\tau_a}^E + \sigma_{\tau_a}^A,$ (3)

$\sigma_{\eta_{f_a}} = \sigma_{\eta_{f_a}}^E + \sigma_{\eta_{f_a}}^A,$ (4)

$\sigma_{m_{i_a}} = \sigma_{m_{i_a}}^E + \sigma_{m_{i_a}}^A,$ (5)

where $\sigma_{\tau_a}^E$, $\sigma_{\eta_{f_a}}^E$, and $\sigma_{m_{i_a}}^E$ are the standard deviations of τ_a, η_{f_a}, and m_{i_a}, respectively, estimated from the ensemble. $\sigma_{\tau_a}^A$, $\sigma_{\eta_{f_a}}^A$, and $\sigma_{m_{i_a}}^A$ are the same as those of the model absolute error.

140   $\sigma_{\tau_a}^A$ is set to $\sigma_{\tau_a}^G$ or $\sigma_{\tau_a}^M$ (whichever is larger) as follows:

$$\sigma_{\tau_a}^A = \begin{cases} \sigma_{\tau_a}^G & if \ \sigma_{\tau_a}^G \geq \sigma_{\tau_a}^M \\ \sigma_{\tau_a}^M & else \end{cases},$$ (6)

where $\sigma_{\tau_a}^G$ is the Root Mean Square Error (RMSE) of the model's τ from ground observation (0.447 in Fig. 6 (c)), and $\sigma_{\tau_a}^M$ is the standard deviation of τ for five years as calculated by the free run model without assimilation. The free run model's spatial resolution is around 1.2 degrees, and the standard deviation is calculated for spring (March, April and May), summer

145   (June, July and August), autumn (September, October and November), and winter (December, January and February) (Fig. 3). $\sigma_{\eta_{f_a}}^A$ (0.110) is calculated from RMSE of the model's α (0.233 in Fig. 6 (f)), which is uniquely determined by η_f. $\sigma_{m_{i_a}}^A$ is set to 0.5 because m_i takes a value from 0. to 1, and ω (which is uniquely determined by m_i) has no correlation with the ground observation data (Fig. 6 (i)). As the non-diagonal component of $\boldsymbol{S_a^A}$ cannot currently be calculated from our limited database, we assume that the correlation from $\boldsymbol{S_a}$ and $\boldsymbol{S_a^E}$ is the same, and calculate the non-diagonal component of $\boldsymbol{S_a}$ as

150   follows:

$$\sigma_{\tau_a \eta_{f_a}} = \frac{\sigma_{\tau_a} \cdot \sigma_{\eta_{f_a}}}{\sigma_{\tau_a}^E \cdot \sigma_{\eta_{f_a}}^E} \sigma_{\tau_a \eta_{f_a}}^E,$$ (7)

$$\sigma_{\tau_a m_{i_a}} = \frac{\sigma_{\tau_a} \cdot \sigma_{m_{i_a}}}{\sigma_{\tau_a}^E \cdot \sigma_{m_{i_a}}^E} \sigma_{\tau_a m_{i_a}}^E,$$ (8)

$$\sigma_{\eta_{f_a}\sigma_{m_{i_a}}} = \frac{\sigma_{\eta_{f_a}} \cdot \sigma_{m_{i_a}}}{\sigma_{\eta_{f_a}}^E \cdot \sigma_{m_{i_a}}^E} \sigma_{\eta_{f_a}}^E \sigma_{m_{i_a}}. \tag{9}$$

155

3 Results and Discussion

3.1 Results of application to Himawari-8

We applied the methodology described in Section 2 to the Himawari-8/AHI. We retrieved τ, η_f and m_i, and then derived ω

and α at 10-min. intervals from the calibrated L1 data subsampled at 0.05° using the method described in Section 2. The

160 channels used for the retrieval are same as those used by Yoshida et al. (2018), which are channels 1 (0.46 μm), 2 (0.51 μm),

3 (0.64 μm), 4 (0.86 μm), and 5 (1.6 μm) over land, and channels 4 and 5 over the ocean. As the number of satellite channels

(two) used over the ocean is less than the number of retrieval parameters (three), not all parameters are stably retrieved by

satellite data. Therefore, m_i over the ocean, which is the least sensitive to satellite observation, is set to 0 (i.e., non-absorbing

aerosol) at this time, because the aerosol over the ocean is generally less absorbing than that over land, and using the model's

165 m_{i_a} as m_i over the ocean leads to a worse estimation of τ (not shown). After obtaining a better model m_{i_a} in the future, we

will use the model's m_{i_a} as m_i over the ocean. Note that m_i over land is properly retrieved from satellite data (i.e., not set to

0) using the model's m_{i_a} as a priori estimate, since the number of satellite channels (five) used over land is greater than the

number of retrieval parameters (three).

170 We compare the retrieval results from (b) the new algorithm using $S_a^E + S_a^A$ for S_a, (c) the new algorithm using only S_a^E

for S_a, and (a) the original algorithm in Figs. 4 and 5. Figure 4 depicts the retrieved τ, η_f, and m_i at 0200 UTC on May 19,

2016 when aerosols originating from wildfires at a proximity to Lake Baikal in Russia reached Japan. The model's x_a used

for retrieval in Fig. 4 (b) and (c) is indicated in Fig. 4 (d). The $\sigma_{\tau_a}, \sigma_{\eta_{f_a}}$, and $\sigma_{m_{i_a}}$ used for retrieval in Fig. 4 (b) are shown

in Fig. 4 (e). The white regions denote the area where retrieval is not executed due to the presence of clouds, etc. The 2-h

175 forecasts starting from 0000 UTC on May 19 were assimilated with L3 merged τ at 0300, 0600, and 0900 UTC on May 18,

and at 0000 UTC on May 19, and then used for a priori estimate (Fig. 4 (d)). Figure 5 is the same as Fig. 4 except for another

case at 0500 UTC on May 7, 2017, when Asian dust was observed in Japan. The 5-h forecast starting from 0000 UTC on

May 7 (and assimilated at 0300, 0600, and 0900 UTC on May 6, and at 0000 UTC on May 7) is used for a priori estimate

(Fig. 5 (d)). These short-term forecasts with data assimilation are considered relatively realistic compared to long-term

180 forecasts or a free run without assimilation (Yumimoto et al., 2018). If only model ensemble error is used for S_a (Figs. 4 (c),

5 (c)), that is, the absolute error is not included in S_a, all retrieved parameters (especially η_f and m_i over land) are highly

dependent on a priori estimate (Figs. 4 (d), 5 (d)). However, when using an appropriate S_a containing absolute error, the

retrieved τ, η_f, and m_i are updated by satellite data or remain close to a priori estimate depending on the location (Figs. 4 (b),

5 (b)). Specifically, spatially finer τ distributions than the model forecast are retrieved for cases of both wildfire aerosol (Fig.

185   4 (b)) and Asian dust (Fig. 5 (b)) due to the relatively coarser model horizontal resolution. Similar η_f is retrieved over open

ocean in Fig. 4 (b) and Fig. 5 (b), and the large η_f (i.e., small particle) and small η_f (i.e., large particle) are successfully

retrieved in areas corresponding to wildfire aerosol (Fig. 4 (b)) and Asian dust (Fig. 5 (b)), respectively. This distribution is

also expressed in the forecast model in Fig. 5 (d), but cannot be expressed sufficiently in the forecast model in Fig. 4 (d)

because information about the aerosol particle size (e.g., α, η_f) is not assimilated into the model. That is, by using an

190   appropriate $\mathbf{S_a}$, both the model and satellite data are used for estimating the aerosol parameters. In addition, the local noise in

τ and η_f is apparently reduced for this algorithm (Figs. 4 (b), 5 (b)) as compared with the original algorithm (Figs. 4 (a), 5

(a)). This will be discussed in Subsection 3.2.

3.2 Validation

We conducted a preliminary validation of our method by comparing the retrieved τ, α, and ω from the Himawari-8/AHI

195   with those from ground observation known as the Aerosol Robotic Network (AERONET). AERONET's τ and α were

derived from Level 2.0 quality-assured Version 3 direct sun algorithm data (Giles et al., 2019; O'Neill et al., 2003), and ω

was derived from Version 3 AERONET inversion products (Dubovik and King, 2000a; Dubovik et al., 2000b; Dubovik et al.,

2002a; Dubovik et al., 2002b; Dubovik et al., 2006; Sinyuk et al., 2007). AERNET's ω at 500 nm was calculated from linear

interpolation of ω at 440 nm and 675 nm. In this study, the 60 AERONET sites on the full disk of Himawari-8 were used for

200   the validation. We used the AERONET data averaged over 10 min. of AHI observation time. For our retrieval data, we used

τ, α, and ω estimated from AHI L1 radiance data subsampled at 0.05° nearest to the AERONET sites. Initial validation was

conducted for the characteristic three months (March 2018, June 2018, and February 2019). Long-term validation will be

required in future studies.

205   Figure 6 compares the retrieved τ, α, and ω from the AHI with those from AERONET. For the τ estimations (Fig. 6 (a), (b),

(c)), the root mean square error (RMSE), mean bias (MB), and correlation (0.397, -0.172, and 0.635) from this algorithm

(Fig. 6 (b)) are all better than those (0.447, -0.277, and 0.595) from the model forecast (i.e., a priori estimate) in Fig. 6 (c),

which means that satellite information is very effective for the retrieval of τ. In addition, the RMSE and correlation (0.397

and 0.635) in Fig. 6 (b) are better than those (0.533 and 0.615) without the forecast model (Fig. 6 (a)), which means that the

210   model information is also effective and the improved algorithm shows better performance than the original algorithm. The

MB (-0.172) in Fig. 6 (b) is worse than that (-0.011) in Fig. 6 (a), probably because the large outlier in Fig. 6 (a) is improved

in Fig. 6 (b). Figure 7 shows an example of the retrieval results of the outlier (red asterisks in Fig. 6 (a), (b), and (c)), and

depicts that the outlier of the original algorithm (Fig. 7(a)) is improved in the new algorithm by constraining τ to the model's

τ_a. Thus, integrating the model and satellite information resulted in an improvement of the τ estimations.

215

For the α estimations (Fig. 6 (d), (e), (f)), large variance in the original method is considerably reduced by this method. The RMSE and correlation (0.253 and 0.505) from this algorithm (Fig. 6 (e)) are much better than those (0.461 and 0.225) from the original algorithm without the forecast model (Fig. 6 (d)), which indicates that the new algorithm could improve the precision of α estimations by adding more accurate α (RMSE of 0.233) information from the model. In addition, the MB (-

220 0.086) from this algorithm (Fig. 6 (e)) is better than that (-0.117) from the model forecast (Fig. 6 (f)), due to the improvement of negative bias in the large α in the model forecast. Thus, the new α can be retrieved with good accuracy by utilizing the relatively accurate model's α and correcting the bias by using the satellite data.

For the ω estimations (Fig. 6 (g), (h), (i)), the RMSE and correlation (0.038 and 0.519) from this algorithm (Fig. 6 (h)) are

225 better than those (0.053 and -0.009) from the model forecast (Fig. 6 (i)), which indicates the effectiveness of satellite information for ω retrieval. In addition, while statistic scores (i.e., RMSD, correlation, MB) show little modification, this algorithm improved the slope and intercept of the regression line by introducing the model forecast. This is probably because the model's ω is not very consistent with AERONET (RMSE of 0.053), but less biased (-0.001 of MB) due to the possibility that the model's ω, whose determinants are complex (e.g., different ω for the same type of aerosol), generally reflects reality,

230 but not enough in individual cases. Note that the current system assimilates only total τ (total amount of aerosols), and information about the fraction of fine and absorbing aerosols from the retrieval is not fed back to the model forecast. The improved retrieval accuracy of ω can be expected if the model's ω becomes more realistic in the future, such as by assimilating the satellite's ω to the model. Considering the validation results of τ, α, and ω, this new algorithm effectively improved the retrieval accuracy using information from both the model and the satellite by setting appropriate S_a and S_e.

235 **3.3 Worst-case scenario**

We have shown that the new retrieval algorithm using the forecast of an aerosol transport model improves the retrieval accuracy. However, in order to use this algorithm as an operational system, the effects of the model forecast (a priori estimate) that deviate from reality must be examined, because the model forecast may miss an aerosol event. Therefore, we conducted a sensitivity test to investigate the impact on the retrieval results of using unrealistic forecast as a priori estimate.

240 Figure 8 shows the retrieval results on the same day as in Fig. 4, except for using the forecast on another day (April 27, 2018) as a priori estimate of the retrieval (Fig. 8 (d)). If only S_a^E is used as S_a (Fig. 8 (c)), all parameters (especially η_f and m_i) are retrieved unrealistically by being dependent on the unrealistic a priori estimate. However, when using an appropriate S_a (Eq. (2)), the retrieved parameters are well-updated by satellite data with less dependence on unrealistic a priori estimate (Fig. 7 (b)). Even in such an extremely worst-case scenario, this new algorithm is apparently not significantly

245 worse than the current algorithm, especially where the model forecast is missing an aerosol event, which may occur in the model forecast for natural aerosols (e.g., mineral dust and smoke from biomass burning).

4 Summary

We developed a new aerosol retrieval algorithm combining a numerical aerosol forecast. In the retrieval algorithm, the short-term forecast from an aerosol data assimilation system was used for a priori estimate instead of spatially and temporally

250 constant values. This is the first study that utilizes the assimilated model forecast of aerosol for a priori estimate of the retrieval. We applied this new algorithm to the Himawari-8/AHI and confirmed that the aerosol parameters detectable by satellite sensors were retrieved more accurately (RMSE of 0.397 for τ and 0.038 for ω) than a priori model forecast (RMSE of 0.447 for τ and 0.053 for ω) by adding satellite information. Moreover, the retrieval accuracy was improved (RMSE of 0.397 for τ and 0.253 for α) by using the model forecast as compared with using constant a priori estimates (RMSE of 0.533

255 for τ and 0.461 for α). As a result, retrieval with high accuracy can be performed by effectively using both model and satellite information depending on each covariance. By using the assimilated forecast for a priori estimate, information from previous observations can be propagated to future retrievals, thereby leading to better retrieval accuracy. In this way, satellite observation and model simulation are used synergistically to continuously estimate the optimum field of aerosol. In the future, by applying this methodology to other polar orbit sensors, the observation of geostationary satellites sensors can be

260 utilized for the polar orbit sensors, leading to the combined use of geostationary and polar orbit sensors.

Data availability

Himawari-8/AHI aerosol data are available from JAXA Himawari Monitor site: https://www.eorc.jaxa.jp/ptree/index.html. The retrieved data in this study can be requested directly from the lead author (mayum@restec.or.jp).

265 Author contributions

MY developed retrieval code and analyzed the data with significant conceptual input from KY and critical technical support from TN, MK, and HM. KY and TT prepared the assimilated forecast data for test cases and long-time validations, respectively. MY prepared the manuscript with contributions from all co-authors.

Competing interests

270 The authors declare that they have no conflict of interest.

Acknowledgements

The authors are grateful to the Open CLASTER project for allowing us to use the RSTAR package for this research. We would like to thank the AERONET project and its staff for establishing and maintaining the AERONET sites considered in this investigation. We also thank Dr. Haruma Ishida for providing the cloud detection algorithm (CLAUDIA). Finally, we
275 appreciate the valuable discussions and support provided by Mr. Takashi Maki, Dr. Tsuyoshi Sekiyama, Dr. Makiko Hashimoto, and Prof. Teruyuki Nakajima. This study was supported by JSPS Grants-in-Aid for Scientific Research JP16H02946, and the JAXA/GCOM-C project.

References

Benedetti, A., Morcrette, J.-J., Boucher, O., Dethof, A., Engelen, R. J., Fisher, M., Flentje, H., Huneeus, N., Jones, L.,
280 Kaiser, J. W., Kinne, S., Mangold A., Razinger, M. , Simmons, A. J., Suttie, M.: Aerosol analysis and forecast in the European Centre for Medium-Range Weather Forecasts Integrated Forecast System: 2. Data assimilation, J. Geophys. Res., 114, D13205, doi:10.1029/2008JD011115, 2009.

Bessho, K., Date, K., Hayashi, M., Ikeda, A., Imai, T., Inoue, H., Kumagai, Y., Miyakawa, T., Murata, H., Ohno, T., Okuyama, A., Oyama, R., Sasaki, Y., Shimazu, Y., Shimoji, K., Sumida, Y., Suzuki, M., Taniguchi, H., Tsuchiyama, H.,
285 Uesawa, D., Yokota, H., and Yoshida R.: An introduction to Himawari-8/9 - Japan's new-generation geostationary meteorological satellites. J. Meteor. Soc. Japan, 94, 151-183, 2016.

Dai, T., Cheng, Y., Suzuki, K, Goto, D., Kikuchi, M., Schutgens, N., Yoshida, M., Zhang, P., Husi, L., Guangyu, S., and Nakajima, T.: Hourly aerosol assimilation of Himawari-8 AOT using the four-dimensional local ensemble transform Kalman filter, Journal of Advances in Modeling Earth Systems, 11, 680–711, https://doi.org/10.1029/ 2018MS001475, 2019.

290 Dai, T., Schutgens, N. A. J., Goto, D., Shi, G., and Nakajima T.: Improvement of aerosol optical properties modeling over Eastern Asia with MODIS AOD assimilation in a global non-hydrostatic icosahedral aerosol transport model, Environ. Pollut., 195, 319–329, doi:10.1016/j.envpol.2014.06.021, 2014.

Dubovik, O. and King, M. D.: A flexible inversion algorithm for retrieval of aerosol optical properties from Sun and sky radiance measurements, J. Geophys. Res., 105, 20,673-20,696, 2000a.

295 Dubovik, O., Sinyuk, A., Lapyonok, T., Holben, B. N., Mishchenko, M., Yang, P., Eck, T. F., Volten, H., Munoz, O., Veihelmann, B., van der Zander, Sorokin, M., and Slutsker I., Application of light scattering by spheroids for accounting for particle non-sphericity in remote sensing of desert dust, J. Geophys. Res., 111, D11208, doi:10.1029/2005JD006619, 2006.

Dubovik, O., Smirnov, A., Holben, B. N., King, M. D., Kaufman, Y. J., Eck, T. F., and Slutsker, I.: Accuracy assessment of aerosol optical properties retrieval from AERONET sun and sky radiance measurements, J. Geophys. Res., 105, 9791-9806,
300 2000b.

Dubovik, O., Holben, B. N., Eck, T. F., Smirnov, A., Kaufman, Y. J., King, M. D., Tanré, D., and Slutsker, I.: Variability of absorption and optical properties of key aerosol types observed in worldwide locations, J. Atmos. Sci., 59, 590-608, 2002b.

Dubovik, O., Holben, B. N., Lapyonok, T., Sinyuk, A., Mishchenko, M. I., Yang, P., and Slutsker, I.: Non-spherical aerosol retrieval method employing light scattering by spheroids, Geophys. Res. Lett., 10, 10.1029/2001GL014506, 2002a.

305 Fukuda, S., Nakajima, T., Takenaka, H., Higurashi, A., Kikuchi, N., Nakajima, T. Y., and Ishida, H.: New approaches to removing cloud shadows and evaluating the 380 nm surface reflectance for improved aerosol optical thickness retrievals from the GOSAT/TANSO-Cloud and Aerosol Imager, Journal of Geophysical Research: Atmospheres, 118, 13-520, 2013.

Giles, D. M., Sinyuk, A., Sorokin, M. G., Schafer, J. S., Smirnov, A., Slutsker, I., Eck, T. F., Holben, B. N., Lewis, J. R., Campbell, J. R., Welton, E. J., Korkin, S. V., and Lyapustin, A. I.: Advancements in the Aerosol Robotic Network

310 (AERONET) Version 3 database – automated near-real-time quality control algorithm with improved cloud screening for Sun photometer aerosol optical depth (AOD) measurements, Atmos. Meas. Tech., 12, 169-209, https://doi.org/10.5194/amt-12-169-2019, 2019.

Granier, C., Bessagnet, B., Bond, T., D'Angiola, A., Denier van der Gon, H., Frost, G. J., Heil, A., Kaiser, J. W., Kinne, S., Klimont, Z., Kloster, S., Lamarque, J.-F., Liousse, C., Masui, T., Meleux, F., Mieville, A., Ohara, T., Raut, J.-C., Riahi, K.,

315 Schultz, M. G., Smith, S. J., Thompson, A., van Aardenne, J., van der Werf, G. R., and van Vuuren, D. P., Evolution of anthropogenic and biomass burning emissions of air pollutants at global and regional scales during the 1980–2010 period, Climatic Change, 109, 163-190, 10.1007/s10584-011-0154-1, 2011.

Higurashi, A., and Nakajima T.: Development of a two-channel aerosol retrieval algorithm on a global scale using NOAA AVHRR, J. Atmos. Sci., 56, 924-941, 1999.

320 Hsu, N. C., Tsay, S.-C., King, M. D., and Herman J. R.: Aerosol properties over bright-reflecting source regions, IEEE Trans. Geosco. Remote Sens., 42, 557-569, 2004.

IPCC, Climate Change: Synthesis Report. Contribution of Working Groups I, II and III to the Fifth Assessment Report of the Intergovernmental Panel on Climate Change [Core Writing Team, R. K. Pachauri and L. A. Meyer (eds.)], Geneva, Switzerland, 151 pp, 2014.

325 Jeong, U., Kim, J., Ahn, C., Torres, O., Liu, X., Bhartia, P. K., Spurr, R. J. D., Haffner, D., Chance, K., and Holben, B. N.: An optimal-estimation-based aerosol retrieval algorithm using OMI near-UV observations, Atmos. Chem. Phys., 16, 177–193, https://doi.org/10.5194/acp-16-177-2016, 2016.

Jin, J., Segers, A., Heemink, A., Yoshida, M., Han, W., and Lin, H.-X: Dust emission inversion using Himawari-8 AODs over East Asia: An extreme dust event in May 2017, Journal of Advances in Modeling Earth Systems, 11, 446–467,

330 https://doi.org/10.1029/2018MS001491, 2019.

Kaiser, J. W., Heil, A., Andreae, M. O., Benedetti, A., Chubarova, N., Jones, L., Morcrette, J. J., Razinger, M., Schultz, M. G., Suttie, M., and van der Werf, G. R.: Biomass burning emissions estimated with a global fire assimilation system based on observed fire radiative power, Biogeosciences, 9, 527-554, 10.5194/bg-9-527-2012, 2012.

Kaufman, Y. J., Tanré, D., Remer, L. A., Vermote, E. F., Chu, A., and Holben B. N.: Operational remote sensing of

335 tropospheric aerosol over land from EOS moderate resolution imaging spectroradiometer, Journal of Geophysical Research: Atmospheres, 102, 17051-17067, 1997.

Kikuchi M., Murakami, H., Suzuki, K., Nagao, T. M., and Higurashi A.: Improved Hourly Estimates of Aerosol Optical Thickness using Spatiotemporal Variability Derived from Himawari-8 Geostationary Satellite, IEEE Trans. Geosci. Remote Sensing, 2018, doi: 10.1109/TGRS.2018.2800060, 2018.

340 Lee, S., Song, C. H., Park, R. S., Park, M. E., Han, K. M., Kim, J., Choi, M., Ghim, Y. S., and Woo J.-H.: GIST-PM-Asia v1: development of a numerical system to improve particulate matter forecasts in South Korea using geostationary satellite-retrieved aerosol optical data over Northeast Asia, Geosci. Model Dev., 9(1), 17– 39, doi:10.5194/gmd-9-17-2016, 2016..

Levy, R. C., Remer, L. A., Mattoo, S., Vermote, E. F., and Kaufman Y. J.: Second-generation operational algorithm: Retrieval of aerosol properties over land from inversion of Moderate Resolution Imaging Spectroradiometer spectral
345 reflectance, J. Geophys. Res., 112, D13211, doi:10.1029/2006JD007811,2007.

O'Neill, N. T., Eck, T. F., Smirnov, A., Holben, B. N., and Thulasiraman, S.: Spectral discrimination of coarse and fine mode optical depth, J. Geophys. Res., Vol. 108, No. D17, 4559-4573, 10.1029/2002JD002975, 2003.

Remer, L. A., Kaufman, Y. J., Tanré, D., Mattoo, S., Chu, D. A., Martins, J. V., R.-R. Li, Ichoku, C., Levy, R. C., Kleidman, R. G., Eck, T. F., Vermote, E., and Holben B. N.: The MODIS aerosol algorithm, products, and validation, Journal of the
350 Atmospheric Sciences, 62, 947-973, 2005.

Rubin, J. I., Reid, J. S., Hansen, J. A., Anderson, J. L., Collins, N., Hoar, T. J., Hogan, T., Lynch, P., McLay, J., Reynolds, C. A., Sessions, W. R., Westphal, D. L., Zhang, J.: Development of the Ensemble Navy Aerosol Analysis Prediction System (ENAAPS) and its application of the Data Assimilation Research Testbed (DART) in support of aerosol forecasting, Atmos. Chem. Phys. Discuss., 15(20), 28,069–28,132, doi:10.5194/acpd-15-28069-2015, 2015.

355 Saide, P. E., G. R. Carmichael, Z. Liu, C. S. Schwartz, H. C. Lin, A. M. da Silva, and E. Hyer (2013), Aerosol optical depth assimilation for a size-resolved sectional model: Impacts of observationally constrained, multi-wavelength and fine mode retrievals on regional scale analyses and forecasts, Atmos. Chem. Phys., 13(20), 10, 425–10,444, doi:10.5194/acp-13-10425-2013.

Saide, P. E., Kim, J., Song, C. H., Choi, M., Cheng, Y. and Carmichael, G. R.: Assimilation of next generation geostationary
360 aerosol optical depth retrievals to improve air quality simulations, Geophys. Res. Lett., 41, 9188–9196, doi:10.1002/2014GL062089, 2014.

Sinyuk, A., Dubovik, O., Holben, B., Eck, T. F., Breon, F-M., Martonchik, J., Kahn, R., Diner, D. J., Vermote, E. F., Roger, J-C., Lapyonok, T., and Slutsker, I.: Simultaneous retrieval of aerosol and surface properties from a combination of AERONET and satellite, Rem. Sens. of Env., 107, doi:10.1016/j.rse.2006.07.022, 2007.

365 Tanaka, T. Y., and Chiba M.: Global simulation of dust aerosol with a chemical transport model, MASINGAR. J. Meteorol. Soc. Japan, 83A, 255–278, doi:10.2151/jmsj.83A.255, 2005.

Tanaka, T. Y., Orito, K., Sekiyama, T. T., Shibata, K., Chiba, M., and Tanaka, H.: MASINGAR, a global tropospheric aerosol chemical transport model coupled with MRI/JMA98 GCM: Model description, Pap. Meteorol. Geophys., 53, 119-138, 10.2467/mripapers.53.119, 2003.

370   Xian, P., Reid, J. S., Hyer, E. J., Sampson, C. R., Rubin, J. I., Ades, M., Asencio, N., Basart, S., Benedetti, A., Bhattacharjee, P., Brooks, M. E., Colarco, P. R., Da Silva, A., Eck, T. F., Guth, J., Jorba, O., Kouznetsov, R., Kipling, Z., Sofiev, M., Carcia-Pando, C. P., Pradhan, Y., Tanaka, T., Wang, J., Westphal, D. L., Yumimoto, K. and Zhang, J.: Current State of the global operational aerosol multi-model ensemble: an update from the International Cooperative for Aerosol Prediction (ICAP), Q. J. R. Meteorol. Soc., qj.3497, doi:10.1002/qj.3497, 2019.

375   Yoshida, M, Kikuchi, M., Nagao, T. M., Murakami, H., Nomaki, T., and Higurashi, A.: Common retrieval of atmospheric aerosol properties for imaging satellite sensors, Journal of the Meteorological Society of Japan, doi:10.2151/jmsj. 2018-039, 2018.

       Yukimoto, S., Adachi, Y., Hosaka, M., Sakami, T., Yoshimura, H., Hirabara, M., Tanaka, T. Y., Shindo, E., Tsujino, H., Deushi, M., Mizuta, R., Yabu, S., Obata, A., Nakano, H., Koshiro, T., Ose, T., and Kitoh, A.: A new global climate model of

380   the Meteorological Research Institute: MRI-CGCM3 – model description and basic performance, J. Meteorol. Soc. Japan, 90A, 23–64, doi:10.2151/jmsj.2012-A02, 2012.

       Yumimoto, K., Mura kami, H., Yanaka, T. Y., Sekiyama, T. T., Ogi, A., and Maki T.: Forecasting of Asian dust storm that occurred on May 10–13, 2011, using an ensemble-based data assimilation system, Particuology, doi:10.1016/j.partic.2015.09.001, 2015.

385   Yumimoto, K., Nagao, T. M., Kikuchi, M., Sekiyama, T. T., Murakami, H., Tanaka, T. Y., and Maki, T.: Aerosol data assimilation using data from Himawari-8, a next-generation geostationary meteorological satellite, Geophysical Research Letters, 43(11), 5886-5894, https://doi.org/10.1002/2016GL069298, 2016.

       Yumimoto, K., Tanaka, T. Y., Oshima, N., and Maki T.: JRAero: the Japanese Reanalysis for Aerosol v1.0, Geosci. Model Dev., 10, 3225–3253, 2017.

390   Yumimoto, K., Tanaka, T., Yoshida, M, Kikuchi, M., Nagao, T. M., Murakami, and H., Maki, T.: Assimilation and Forecasting Experiment for Heavy Siberian Wildfire Smoke in May 2016 with Himawari-8 Aerosol Optical Thickness, Journal of the Meteorological Society of Japan, doi:10.2151/jmsj. 2018-035, 2018.
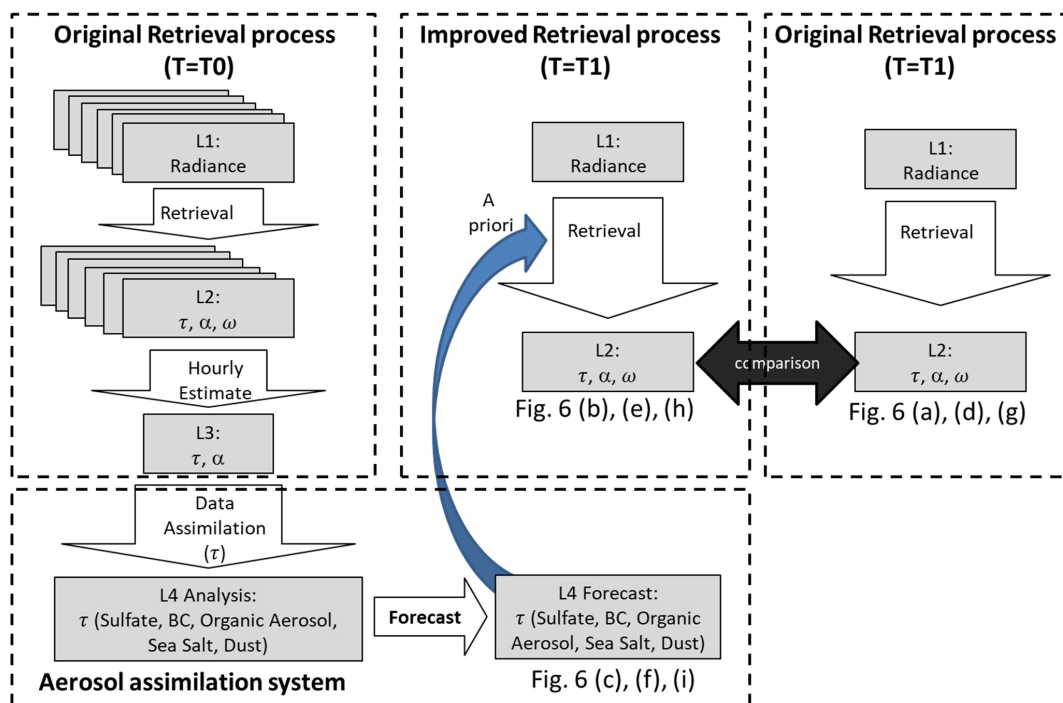
Figure 1: Flowchart of data processing for aerosol retrieval at time T1.
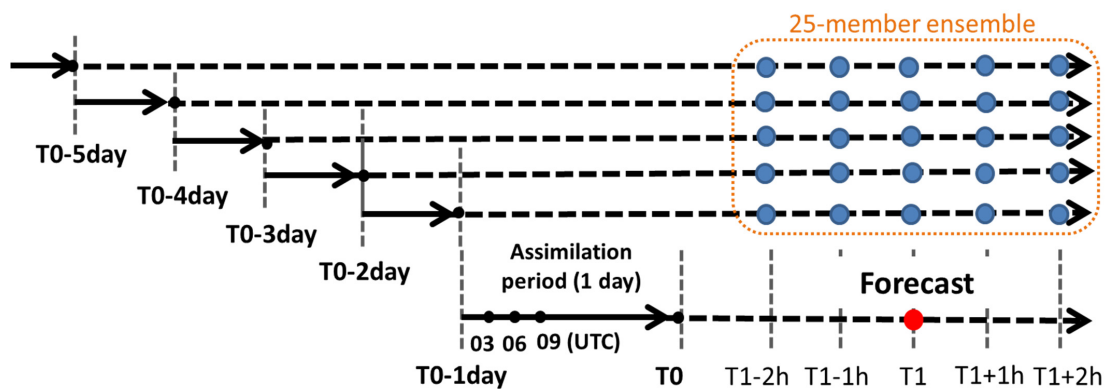
Figure 2: Forecast of aerosol transport model used for retrieval at time T1. Solid and dashed lines show the assimilation period (1 day) and forecast run, respectively.
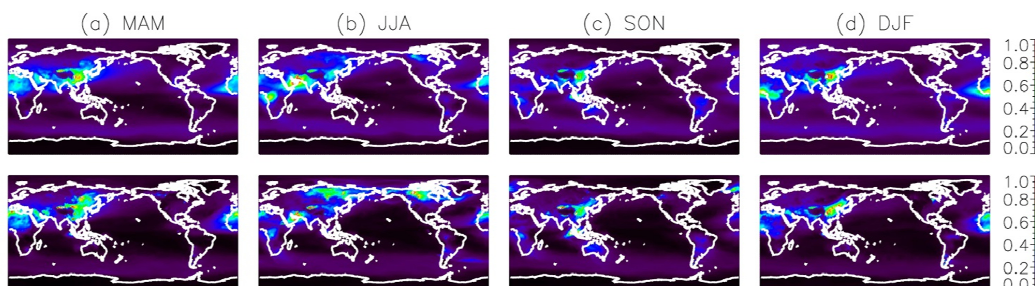
400

Figure 3: Mean (upper) and standard deviation (lower) of τ for free run model from 2011 to 2015 in (a) March, April and May, (b) June, July and August, (c) September, October and November, and (d) December, January and February.
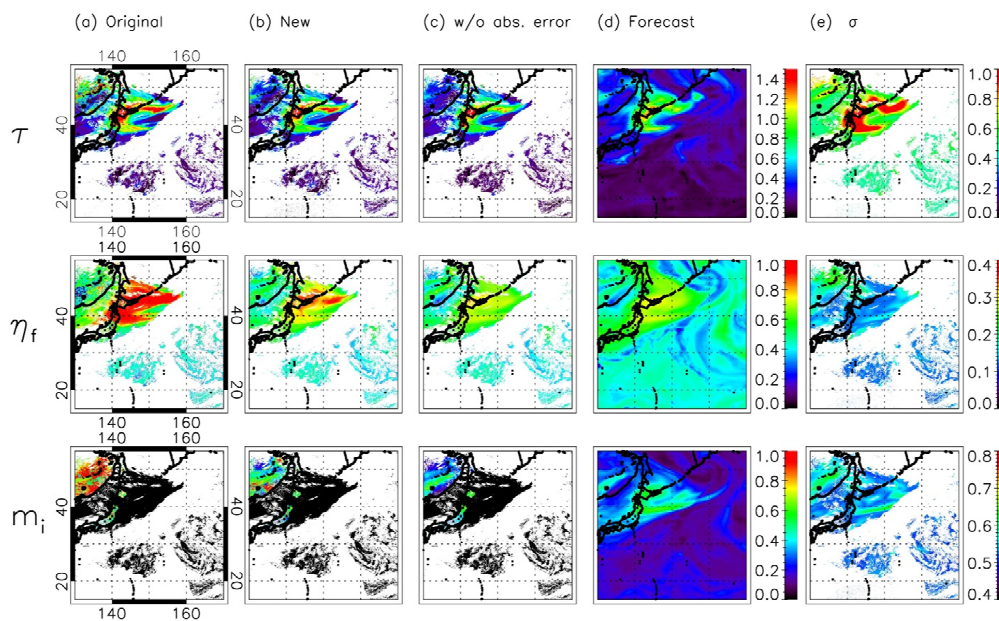
405   **Figure 4: aerosol optical thickness at 500 nm τ (upper), external mixing ratio of dry volume concentration for fine particles η_f (middle), and imaginary part of refractive index for fine mode m_i (lower) that are (a) retrieved from the original algorithm (i.e., using constant a priori estimate), (b) retrieved from this algorithm, (c) retrieved from this algorithm but without model absolute error (S_a^A), and (d) from the model forecast at 0200 UTC on May 19, 2016. (e) standard deviations of model forecast (σ_{τ_a}, $\sigma_{\eta_{f_a}}$, and $\sigma_{m_{i_a}}$) used for retrieval in (b).**

410
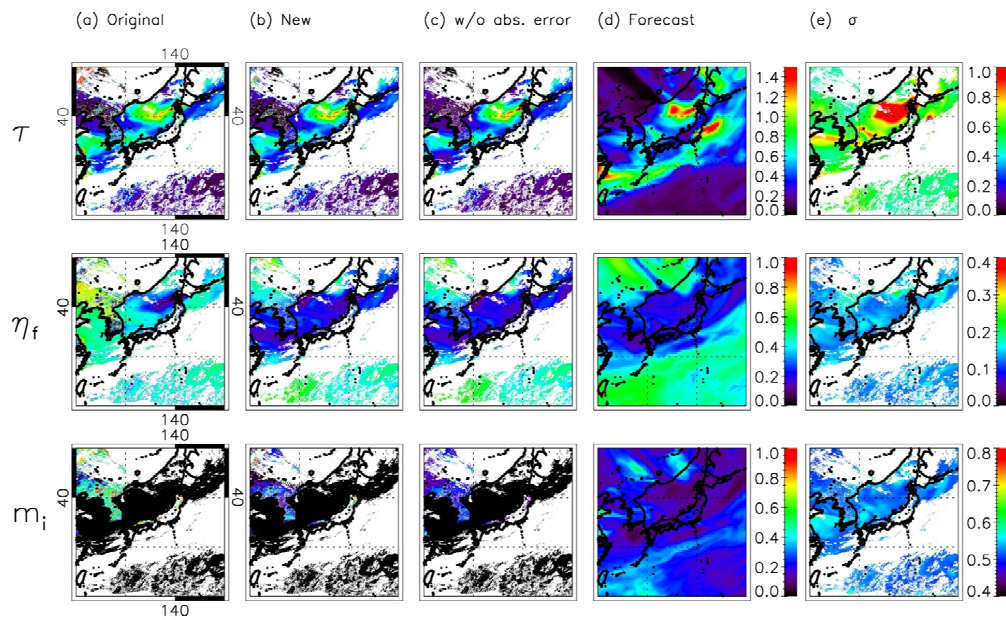
Figure 5: Same as Fig. 4, except for the case at 0500 UTC on May 7, 2017.
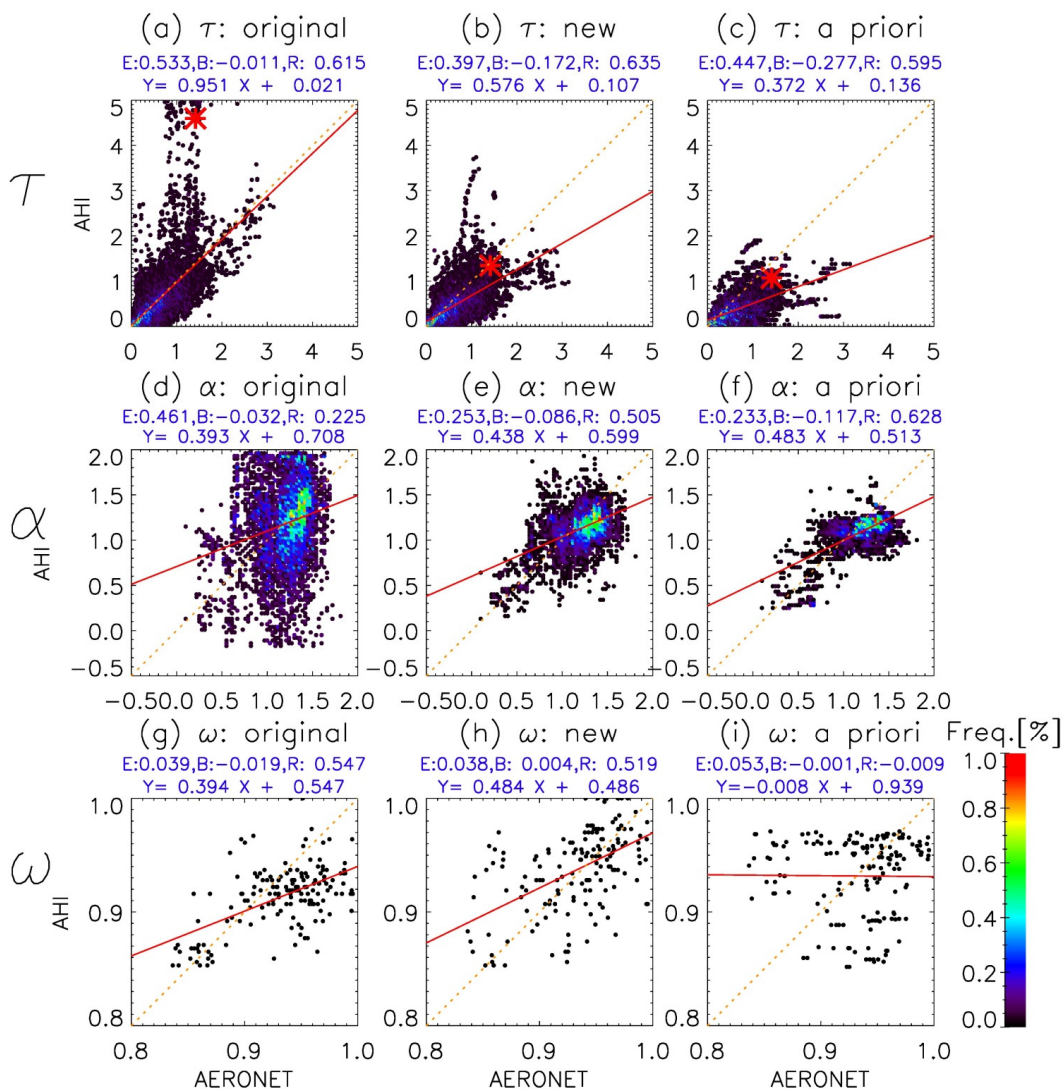
Figure 6: Frequency distribution of τ (a, b, c), a (d, e, f), and ω (g, h, i) retrieved from AHI and those from AERONET. (a), (d), and (g) show the results from the original algorithm (i.e., using constant a priori), (b), (e), and (h) show the results from this algorithm, and (c), (f), and (i) are a priori estimate used for (b), (e), and (h), respectively. E, B, and R above the figures show the root mean square error, mean bias, and correlation, respectively. Red asterisks in (a), (b), and (c) show the results at asterisks in Fig. 7 (a) and (b).

420
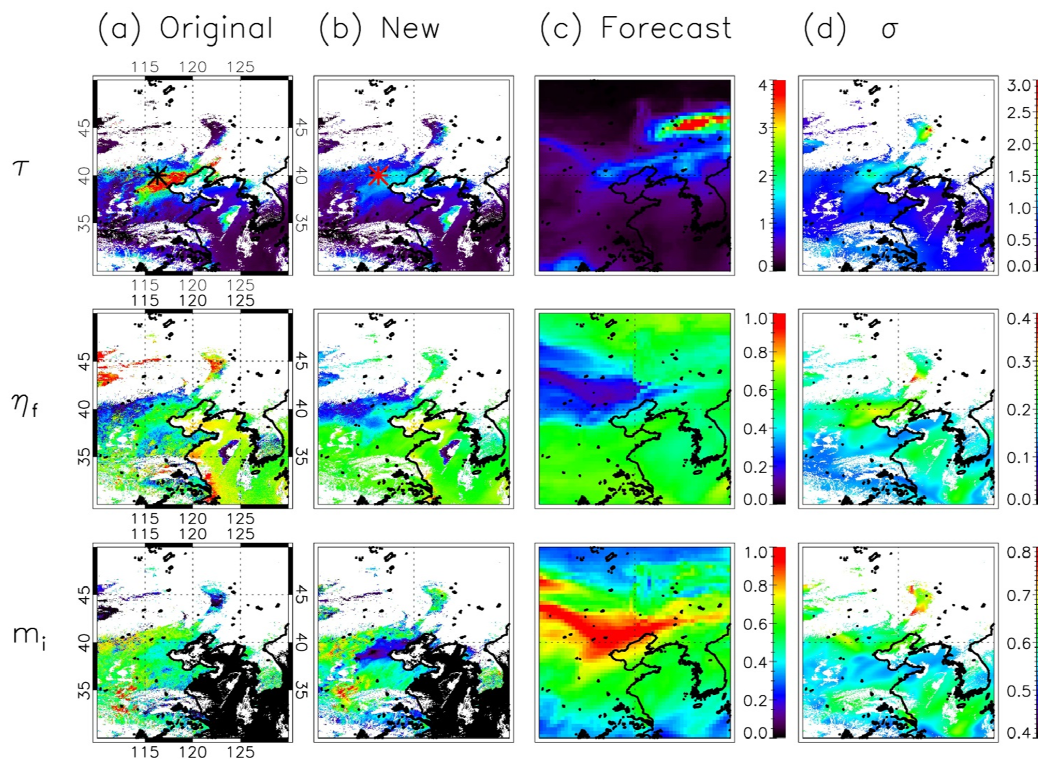
Figure 7: aerosol optical thickness at 500 nm τ (upper), external mixing ratio of dry volume concentration for fine particles η_f (middle), and imaginary part of refractive index for fine mode m_i (lower) that are (a) retrieved from the original algorithm (i.e., using constant a priori estimate), (b) retrieved from this algorithm, and (c) from the model forecast at 0710 UTC on March 13, 2018. (d) standard deviations of model forecast (σ_{τ_a}, $\sigma_{\eta_{f_a}}$, and $\sigma_{m_{i_a}}$) used for retrieval in (b). Black and red asterisks in (a) τ and (b) τ, respectively, show the results for red asterisks in Fig. 6 (a), (b), and (c).
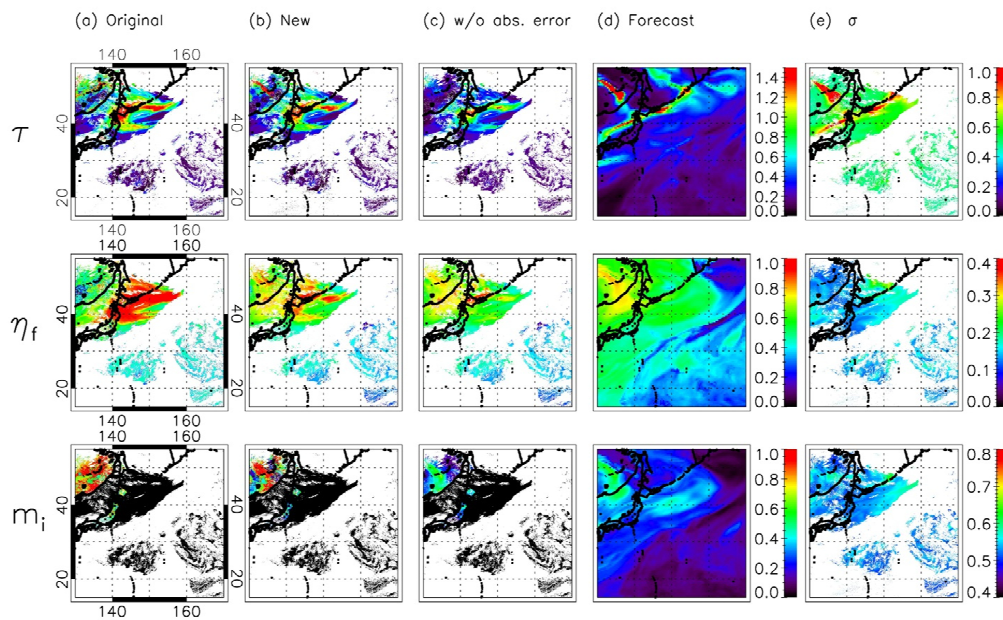
430 **Figure 8:** Same as Fig. 4, except for using the forecast on April 27, 2018 as a priori estimate.